Journal of Atmospheric and Solar–Terrestrial Physics 230 (2022) 105843

Contents lists available at ScienceDirect

Journal of Atmospheric and Solar-Terrestrial Physics

journal homepage: www.elsevier.com/locate/jastp

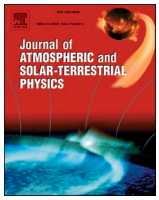

Research Paper

Data-based optimization of a simple shortwave fadeout absorption model

R.A.D. Fiori [a,*], S. Chakraborty [b], L. Nikitina [a]

[a] Canadian Hazards Information Service, Natural Resources Canada, Ottawa, Ontario, Canada
[b] Bradley Department of Electrical and Computer Engineering, Virginia Tech, Blacksburg, VA, USA

ARTICLE INFO

Keywords:
Shortwave fadeout
Ionospheric HF absorption
HF absorption Model
HF radiowave Propagation

ABSTRACT

Electron density enhancement caused by electromagnetic radiation emitted during a solar X-ray flare has the potential to increase high frequency (HF; 3–30 MHz) absorption in the dayside D-region ionosphere, impacting shortwave radio signals by reducing the signal strength, a phenomenon commonly referred to as shortwave fadeout. Data-based optimization of a simple absorption model is performed incorporating solar X-ray flux data and 30 MHz riometer data from stations distributed across Canada. In a single event study the data-based optimization model is shown to overestimate absorption by 1% for the duration of an X2.1 solar X-ray flare. This corrects an underestimation by the NOAA D-region Absorption Prediction (D-RAP) model. In a statistical study, based on 87 events, data-based optimization performed on an event-by-event basis showed excellent overall agreement between measured and modelled data: the Pearson correlation coefficient was R = 0.88, and the slope of the best-fit line to the data was m = 0.91. A generalized model was developed using data from all 87 events collectively. Although good agreement was found between the measured and modelled data sets, correlation and slope were slightly reduced to R = 0.75 and m = 0.80. Model accuracy is characterized by prediction efficiency (PE) which peaked at PE = 0.78 for the event-by-event evaluation and PE = 0.48 for the collective data set. The results of this study highlight the advantages of data-based optimization in modelling absorption due to shortwave fadeout.

1. Introduction

A solar X-ray flare is a sudden release of energy causing a brightening of the Sun's photosphere, the emission of electromagnetic radiation, and in some cases the emission of energetic charged particles (e.g., Davies, 1990; Mitra, 1974). The electromagnetic radiation emitted during a solar flare, most notably in X-ray and extreme ultraviolet (EUV) bands, reaches the Earth within approximately 8 min causing increased electron density in the dayside or sunlit ionosphere, and a reduction in altitude of the base of the ionosphere (Belrose and Cetiner, 1962; Davies, 1990).

Changes to the ionospheric electron density profile strongly impact high frequency (HF; 3–30 MHz) radiowave propagation by determining whether a signal of a given frequency will refract through or reflect from the upper E and F region of the ionosphere, be transmitted through the entire ionosphere, or be absorbed in the D-region ionosphere. D-region absorption is caused by the loss of the signal energy as heat through collisions with D-region particles, causing a partial or complete reduction in the strength of the radio signal (e.g., Browne et al., 1995).

Enhancements in absorption caused by increased photoionization on the sunlit side of the Earth following a solar X-ray flare potentially impacts shortwave radio signals by reducing the signal strength, a phenomenon commonly referred to as shortwave fadeout (SWF) (e.g., Mitra, 1974). SWF is characterized by a sudden reduction in an HF radio signal lasting on the order of minutes to hours, similar to the timescale and structure of the associated solar X-ray flux enhancements (Davies, 1990). The radiation increases ionization in the dayside ionosphere, most predominately at equatorial latitudes close to the Earth's subsolar point and falls off toward the nightside (Fiori et al., 2018; Schumer, 2009). SWF is an important topic of research due to its clear impacts to over-the-horizon radar (OTHR) used for long-range surveillance (Thayaparan et al., 2018), and to HF radio communication used by, for example, the military, aviation, emergency management, and shipping industries (e.g., Agy, 1970; Cannon et al., 2013; Coyne, 1979; Knipp et al., 2021; National Research Council, 2008; Neal et al., 2013; Pirjola et al., 2005).

The impact of SWF on HF radiowave propagation is clearly demonstrated in signatures of the Super Dual Auroral Radar Network

* Corresponding author.
E-mail address: robyn.fiori@nrcan-nrcan.gc.ca (R.A.D. Fiori).

https://doi.org/10.1016/j.jastp.2022.105843
Received 15 October 2021; Received in revised form 22 February 2022; Accepted 22 February 2022
Available online 24 February 2022

(SuperDARN) which uses 8–18 MHz radio signals to study the ionosphere (Chisham et al., 2007). Operating continuously, with a field of view that covers a large portion of the Northern and Southern high and mid-latitude ionosphere, SuperDARN is an important instrument for monitoring HF radiowave propagation. Absorption due to increased ionization caused by solar X-ray flares changes HF propagation conditions (e.g., Danskin et al., 2002) and can cause a partial or complete signal loss (e.g., Chakraborty et al., 2018; Fiori et al., 2018), a drop in the decameter sky noise (i.e., background radio noise) (Berngardt et al., 2018; Bland et al., 2018; Chakraborty et al., 2019), and variations in the Doppler shift of echoes (Fiori et al., 2018; Hosokawa et al., 2000; Kikuchi et al., 1986; Watanabe and Nishitani, 2013).

Frissell et al. (2014) and Frissell et al. (2019) demonstrate the impact of solar X-ray flares to HF radiowave propagation based on data from two amateur radio reporting networks: the Reverse Beacon Network (RBN) and the Weak Signal Propagation Reporting Network (WSPRNet). In Frissell et al. (2014), the response of RBN data to an X2.1 solar X-ray flare is analyzed. Using data in 6 bands spanning 1.8 MHz–28 MHz, they show that following the flare, the number of available propagation paths drops to 35% of the pre-flare number, with the strongest impacts observed at the lowest frequencies. Frissell et al. (2019) examines the response of RBN and WSPRNet data to a series of space weather events observed 4–14 September 2017. At Caribbean latitudes (roughly 15°–30° geographic latitude), X-class solar X-ray flares on 6, 7, and September 10, 2017 were shown to cause abrupt losses in 7 MHz and 14 MHz signals lasting on the order of tens of minutes to hours. These frequencies are used for HF emergency communications which impacted hurricane relief efforts associated with major storms observed during this period, including Hurricane Irma and Jose. Redmon et al. (2018) provides several examples of the practical impact of the loss of HF radio communications during this event.

Chakraborty et al. (2018) characterize the typical signature of the impact of solar X-ray flares at 10–12 MHz using an epoch-style analysis of daytime SuperDARN observations. Based on an analysis of 9 events, they observed a 3-phase response in the number of ground scattered echoes following a solar X-ray flare. The onset phase was marked by a sudden drop in ground scattered echoes within ~100 s. The second phase was characterized by a severe-to-complete signal loss lasting ~10 min, followed by a ~30-min recovery. The severity and duration of the impact was most strongly linked to the solar zenith angle (SZA) of the region impacted; impacts were more severe for lower SZA. The strength of the impact was also linked, to a lesser extent, to radar operating frequency and the peak intensity of the solar X-ray flare. Chakraborty et al. (2019) investigate the impact of isolated versus compound solar X-ray flares and observed that the duration of the impact to SuperDARN following a short succession of X-class flares can be much longer (≥4–5 h) than the superposition of isolated events. They attribute the extended ionospheric relaxation time to the slow recovery of the D region electron temperature following a large perturbation, as proposed by Bajcetic et al. (2015). In particular, large temperature increases can change the recombination rates in the D-region, resulting in a relatively long relaxation time. According to Rodger et al. (1998), the functional form of lower ionospheric relaxation time is semi-logarithmic if there are no external excitations within the system during the relaxation period. Despite the fact that this assumption is valid for an isolated flare, the scenario would change for a compound flare (flares occurring in quick succession). It is during the compound flare that the ionosphere is excited by multiple solar flares in rapid succession before fully recovering from the effects of every previous flare, which results in an extended recovery time.

Although probability models exist for predicting the likelihood of a solar X-ray flare (e.g., Barnes et al. (2016), and references within), the propagation of a solar X-ray flare at the speed of light makes forecasting challenging; event onset and detection occur nearly simultaneously. However, efforts have been made to predict impacts to HF radiowave propagation by modelling the attenuation expected for a signal of a defined frequency (e.g., absorption).

Currently, the most widely used model for predicting absorption due to SWF is incorporated into the D Region Absorption Prediction (D-RAP) model, operated by the Space Weather Prediction Center (SWPC) of the National Oceanic and Atmospheric Administration (NOAA) (https://www.swpc.noaa.gov/content/global-d-region-absorption-prediction-documentation, last accessed 03 January 2022). The advantage of D-RAP is its ability to combine absorption from both solar X-ray flares and solar proton events (e.g., polar cap absorption). However, despite this advantage, the D-RAP model has been shown to underestimate observed absorption due to SWF (Schumer, 2009; Levine et al., 2019), which can be largely attributed to a lack of contribution from D-region measurements or models. Modelling by Levine et al. (2019) seeks to improve this through the incorporation of a physics-based model of the D-region and radiation transport in the ionosphere. A more detailed study is underway to understand the basic nature of the SWF phenomena that includes predictions of HF absorption following a solar X-ray flare (Chakraborty et al., 2021).

This paper proposes a simplified absorption model optimized through the incorporation of absorption measurements made by a relative ionospheric opacity meters (riometers). This approach is similar to an approach developed by Rogers and Honary (2015) and applied by Fiori and Danskin (2016) for modelling polar cap absorption over the high-latitude region. The performance of this model is first demonstrated for a single X2.1 flare observed March 11, 2015, and then evaluated for a collection of M and X class flares observed between 2006 and 2017.

2. Data and instrumentation

2.1. Riometer-derived absorption

A riometer characterizes HF absorption by measuring the opacity of the ionosphere to cosmic radio noise from extra-terrestrial sources (Browne et al., 1995; Davies, 1990). HF absorption is determined by evaluating the deviation of the signal voltage measured by the riometer from the quiet day curve, expressed in dB (NORSTAR, 2014).

Fig. 1 and Table 1 indicate the location of a network of 30 MHz

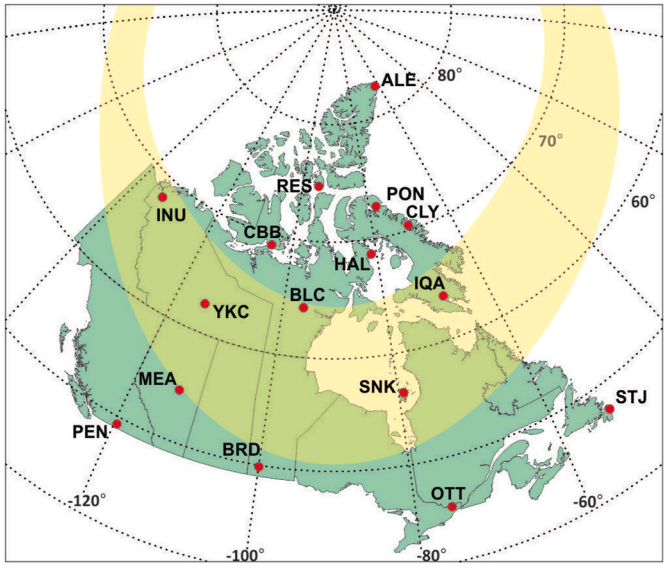

Fig. 1. Location of NRCan riometer stations across Canada (red filled circles). Dashed lines indicated geographic latitude and longitude in increments of 10° of latitude and 20° of longitude. Yellow shading indicates the location of the discrete aurorae using the model of Sigernes et al. (2011) for Kp = 6 calculated for June 01, 2020 at 06:00 UT when Canada was on the nightside. Three-letter station designations are defined in Table 1.

riometers across Canada operated by Natural Resources Canada (NRCan) (Danskin et al., 2008; Lam, 2011). Each riometer has a wide-beam antenna capable of detecting absorption within a ~100 km diameter radius within the ionosphere above the riometer. Data are available at a 1-s resolution and downsampled to a 1-min resolution to be consistent with solar X-ray flux data. The 1-min data were calculated by considering the median absorption observed in the 1-min interval of interest.

2.2. Solar X-ray flux

Solar X-ray flares are classified based on their peak intensity (F_{peak}) in the 0.1–0.8 nm band; A ($F_{peak} < 10^{-7}$ W/m^2); B (10^{-7} W/m$^2 \leq F_{peak} < 10^{-6}$ W/m^2), C (10^{-6} W/m$^2 \leq F_{peak} < 10^{-5}$ W/m^2), M (10^{-5} W/m$^2 \leq F_{peak} < 10^{-4}$ W/m^2), and X ($F_{peak} \geq 10^{-4}$ W/m^2) (Davies, 1990). The B, C, and M categories have 9 subdivisions ranging from, e.g., M1 to M9, where the scaling is defined such that an M2 X-ray flare is twice as powerful as an M1 flare, and an M3 X-ray flare is three times as powerful as an M1 flare. The X category can extend indefinitely and >X9 flares are possible. The largest solar X-ray flare observed (to date) saturated the Geostationary Operational Environmental Satellite Network (GOES) 12 detector on November 04, 2003. The sensor saturated at X17.4, but through careful analysis of riometer data, Brodrick et al. (2005), showed the flare was likely of magnitude X40. Although C-class events can be observed by ground-based instruments (e.g., riometers), M, and especially X, class solar X-ray flares have the most notable features in ground-based observations and the most notable impacts to HF radio propagation (e.g., Contreira et al., 2005).

Solar X-ray flux data were measured by the NOAA/NASA GOES satellite (NASA, 2006) based on measurements from the X-Ray Sensor (XRS) instrument (Machol and Viereck, 2016). Data are available from http://www.ngdc.noaa.gov/stp/satellite/goes/dataaccess.html. In addition to measuring the longer waveband of the solar X-ray spectrum, referred to as the soft X-ray (SXR; 0.1–0.8 nm), the XRS also measures the shorter waveband of the solar X-ray spectrum, referred to as the hard X-ray (HXR; 0.05–0.4 nm). Only SXR data are considered in this study. Data analyzed below are from the GOES 15 satellite, and the SXR data were first divided by a scaling factor of 0.7, following instructions in Machol and Viereck (2016).

Historical data on solar X-ray flares were obtained from NOAA in the form of GOES XRS reports which are available by year from 1975 to 2017 (https://www.ngdc.noaa.gov/stp/space-weather/solar-data/solar-features/solar-flares/x-rays/goes/xrs/). The GOES XRS flare reports are considered the standard solar flare catalogue (e.g., Swalwell et al., 2018), and contain information on flare magnitudes, timing of the start, peak, and end of the flare, and solar coordinates of the eruption.

2.3. Data filtering

Riometers are sensitive instruments that are subject to contamination from a variety of noise sources including voltage spikes from radio noise bursts (e.g., Davies, 1990) and solar radio noise; environmental features caused, for example, by thunderstorms or freezing rain accumulation on the antenna; calibration spikes; and in some cases, instrument errors. Noise was filtered from the riometer data prior to down sampling.

As the focus of this paper is the modelling of SWF-type absorption, additional filtering was performed to remove effects from alternate sources of absorption such as auroral absorption and polar cap absorption (PCA). Auroral absorption was removed by evaluating geomagnetic activity at co-located magnetometer instruments (https://www.spaceweather.gc.ca/plot-tracee/mp-en.php?plot_type=magnetic) and removing data from riometer stations showing absorption roughly correlated with magnetic perturbations (e.g., Fiori et al., 2020). Intervals of PCA were eliminated by closely examining absorption data for solar x-ray flares that occurred during solar proton events (SPEs) identified in the SPE list maintained by the NOAA Space Weather Prediction Center (SWPC) (ftp://ftp.swpc.noaa.gov/pub/indices/SPE.txt). Data for stations where SWF-like absorption signatures were observed concurrently with PCA signatures were removed from the data set.

3. Review of traditional shortwave fadeout models

There are established relationships for determining absorption based on the solar x-ray flux. The D-RAP SWF model is based on work by Stonehocker (1970) who derived a relationship between 10 MHz radio burst electromagnetic flux (E_{radio}, in 10^{-22} W/m^2) and the attenuation (in dB) of a 5 MHz transmission signal. Based on a limited data set consisting of 46 flares observed during summer months (between May and August) from a New Mexico station between 10:00 and 14:00 local time, they observed the attenuation for a 5 MHz signal

$$A(\mathrm{dB}) = (11.33)\log_{10}(E_{\mathrm{radio}}) - 3.333, \quad (1)$$

and reported an error of <9%. These results are limited to the noon sector, during summer months for a single transmission path.

Stonehocker (1970) suggested scaling these results to other frequencies by f^{-2} (citing Schwentek, 1961), and by solar zenith angle SZA, using cos (SZA) to get other propagation paths. Scaling absorption by frequency is reported by Davies (1990) to follow the relationship

$$A_f = \left(\frac{f_1}{f}\right)^z A_{f_1}, \quad (2)$$

where a factor of z is suggested for scaling an observed absorption A_{f_1} of frequency f_1 to the absorption A_f expected for another frequency f. For purely nonderivative absorption, experienced by HF and VHF waves in the D-region ionosphere, a theoretical $z = 2$ relationship is expected, as reported by Stonehocker (1970) and Schwentek (1961). However, in a real-world situation where absorption is not purely non-deviative, z is less well known. Sauer and Wilkinson (2008) suggest a factor of 1.5 to model absorption dependence on frequency, which is used in the D-RAP model, whereas Schumer (2009) recommends a value of 1.24.

Expressions for absorption typically introduce a cos^y (SZA) term to modify their equations based on SZA, but there is a significant discrepancy in the exact power of the cosine term, represented here by y (see Table 2). However, a generalization can be made that absorption is expected to be highest near the sub-solar point and fall off with increasing proximity to the nightside.

The D-RAP model relates the 0.1–0.8 nm solar soft X-ray flux (F, units of W/m^2) observed by the GOES satellite to the attenuation (in dB) at 30 MHz, represented by absorption (A_{DRAP}), through the highest affected frequency (HAF) of a vertical incidence ionogram experiencing 1 dB (or more) of absorption using (https://www.swpc.noaa.gov/content/global

Table 1
Riometer station names, 3-letter abbreviations, geographic latitudes, and geographic longitudes.

Names	Abbreviations	Geographic Latitudes (°N)	Geographic Longitudes (°E)
Alert	ALE	82.5	297.7
Baker Lake	BLC	64.3	264
Brandon	BRD	49.9	260.1
Cambridge Bay	CBB	69.1	255
Clyde River	CLY	70.5	291.5
Hall Beach	HAL	68.8	278.8
Inuvik	INU	68.3	226.5
Iqaluit	IQA	63.7	291.5
Meanook	MEA	54.6	246.7
Ottawa	OTT	45.4	284.5
Penticton	PEN	49.3	240.4
Pond Inlet	PON	72.7	282.1
Resolute Bay	RES	74.7	265.1

Table 2
Values of γ relating absorption and solar zenith angle (SZA) through $\cos^{Y}$ (SZA).

Publications	Y	Comments
Oyinloye (1978) [a]	0.96	morning sector
	0.78	afternoon sector
Bibl et al. (1961)	0.5	
D-RAP	0.75	
Schumer (2009) [b]	0.90	
Davies (1990) [c]	0.85 ± 0.15	low-latitude
	0.5 to 0.9	mid-latitude
	as high as 0.2	auroral zone
Hunsucker and Hargreaves (2003)	0.7 to 1.0	
Stonehocker (1970)	1	
March 11, 2015 (Section 4.1)	1.09 to 1.29	event specific

[a] For absorption experienced by a 2.2 MHz signal.
[b] Based on an analysis of HF signal strength from the HF Investigation of D-region Ionospheric Variation Experiment (HIDIVE) data during solar quiet periods.
[c] Based on a literature review performed by Davies (1990).

-d-region-absorption-prediction-documentation, last accessed January 03, 2022)

$$HAF = (10\log F + 65)\cos^{0.75}(SZA)(\mathrm{MHz}) \tag{3}$$

$$A_{\mathrm{DRAP}} = 0.5\left[\frac{HAF}{F_{abs}}\right]^{1.5}(\mathrm{dB}). \tag{4}$$

Eq. (4) uses an exponent of z = 1.5 to scale absorption at the HAF to absorption at an arbitrary frequency (F_{abs}, in MHz). The factor of 0.5 in Eq. (4) comes from the assumption that absorption is equally divided between the up and down propagation paths. Note that the D-RAP polar cap absorption (PCA) model describes absorption expected for a 30 MHz signal. If the absorption calculated in Eq. (4) is to be added to the PCA model to create a joint SWF/PCA absorption model, then F_{abs} must be 30 MHz.

To demonstrate the performance of the D-RAP SWF model, the March 11, 2015 X2.1 solar X-ray flare peaking at 16:22 UT, presented in Fiori et al. (2018), was chosen for study due to the clear signature observed in absorption data across the network ranging from the middle-latitude OTT station (45.4°) to the high latitude ALE station (82.5°) (see Fig. 3 of Fiori et al. (2018)). Calculations in this section are limited to NRCan riometer stations to ensure instrument consistency for the ALE, BLC, CBB, OTT, PEN, RES, and SNK riometers corresponding to periods where the 0.1–0.8 nm solar X-ray flux exceeded the C1.16 level, identified as the solar X-ray flux at the onset of the solar flare associated enhancement.

Fig. 2a indicates the solar X-ray flux observed by the GOES 15 satellite on March 11, 2015. The X-ray flux began a rapid enhancement at 16:10, crossing the C1.16 level (horizontal dashed line) and reaching a peak value of X2.1 at 16:22 UT. Solar X-ray flux slowly recovered dropping below the C1.16 level at 17:59 UT. The time at which the C1.16 level is crossed is marked by the red dashed vertical lines. Absorption signatures due to SWF (Fig. 2b; solid black line) closely resemble signatures in solar X-ray flux data, namely a sharp enhancement followed by a more gradual recovery. The peak magnitude of the observed absorption enhancement generally drops off with increasing distance from the subsolar point (increasing SZA), similar to electron density enhancements (e.g., Davies 1990; Fiori et al., 2018). Vertical dashed red lines in Fig. 2 at 16:10 UT and 17:59 UT bound the period during which the solar X-ray flux exceeded C1.16 (horizontal dashed black line). The event was long duration, peaking at 16:21 UT. The X2.1 solar X-ray flare was immediately followed by an M-class flare at the end of the plotted interval (not considered in the single event study).

Fig. 2b shows the absorption enhancement observed at OTT in response to the solar X-ray flare. During the 15–19 UT interval shown, SZA at the OTT riometer station began at 57.2°, reached a minimum of 49.0° at 17:12 UT, ending at 54.5°. Absorption reaches a rapid peak of

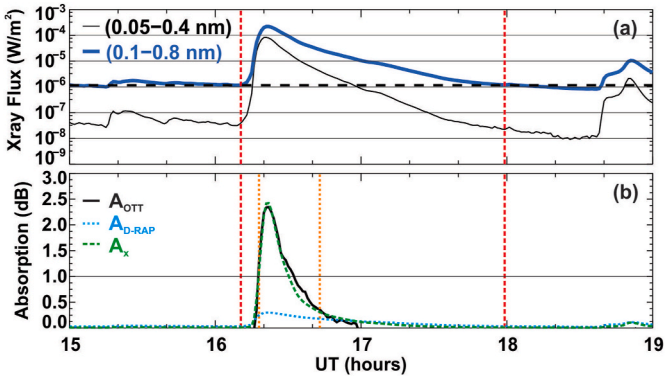

Fig. 2. (a) Solar X-ray flux measured by the GOES 15 satellite on March 11, 2015. Thin black and heavy blue lines represent the 0.05–0.4 nm and 0.1–0.8 nm solar X-ray flux, respectively. Solid horizontal lines indicate magnitudes of 10^{-8}, 10^{-7}, 10^{-6}, 10^{-5}, 10^{-4} W/m^2. The dashed horizontal line at 1.16×10^{-6} Watts m^{-2} (C1.16) identifies the flare start and end times. (b) Absorption at 30 MHz measured by the OTT riometer (solid black line), modelled using D-RAP (dotted blue line), and modelled using the data-optimized approach described in Section 4 (dashed green line) on March 11, 2015. Vertical red bars in (a) and (b) at 16:10 UT and 17:59 UT indicate the period during which the 0.1–0.8 nm solar X-ray flux exceeded C1.16, and there was valid riometer data. The 0.1–0.8 nm solar X-ray flux peaks at X2.1 at 16:22 UT. Vertical orange bars in (b) at 16:18 UT and 16:43 UT indicate where the D-RAP absorption is <50% of the measured absorption.

2.4 dB at 16:22 UT, 1 min after the peak solar X-ray flux, followed by a more gradual recovery. The dotted blue line in Fig. 2b indicates the absorption calculated using the D-RAP model. The modelled absorption does show a minor enhancement at the onset of the enhancement observed at OTT. However, the model significantly underestimates the absorption measured, reaching a peak value of only 0.30 dB, barely passing the 0.1 dB limit commonly used to filter noise from the data. A 30 MHz riometer is able to resolve absorption changes of ~0.1 dB (Davies, 1990). If the data are limited to the period bounded by the red dashed vertical lines where the measured absorption is greater than the 0.1 dB noise threshold, the modelled absorption is on average 49% of the measured value (RMSE = 0.9 dB). If the data are further limited to periods where absorption is > 1 dB, the modelled absorption is, on average, 17% of the measured value (RMSE = 1.4 dB). The largest discrepancy (13%) is observed from 16:20–16:23 UT, at the time of peak absorption. Modelled absorption falls below 50% of the measured value from 16:18 UT to 16:43 UT where the measured absorption is ≥ 0.4 dB (bounded by orange dotted vertical bars in Fig. 2b).

4. Data-based optimization of shortwave fadeout

Recognizing the issues with the D-RAP SWF model at 30 MHz, it becomes apparent that a new model is desirable. Ignoring the frequency scaling introduced in Eq. (4), absorption at 30 MHz (A_x), in dB, is determined based on the solar X-ray flux (F) and solar zenith angle (SZA) from.

$$A_x = [xF + b]\cos(SZA)\ \ (\mathrm{dB}) \tag{5}$$

where x and b are fitting coefficients with units of (m^2 dB/W) and dB, respectively. Furthermore, b is taken to be zero as SWF is not expected to be observed as F goes to zero:

$$A_x = [xF]\cos(SZA)\ \ (\mathrm{dB}). \tag{6}$$

A logarithmic fit was also evaluated, similar to Eq. (3), but better agreement was found without using a logarithm.

Fitting coefficient x is determined using a least-squares fitting for a line through the origin where the independent variable ($F\cos(SZA)$) is taken to have negligible uncertainty and the dependent variable (A_x) has

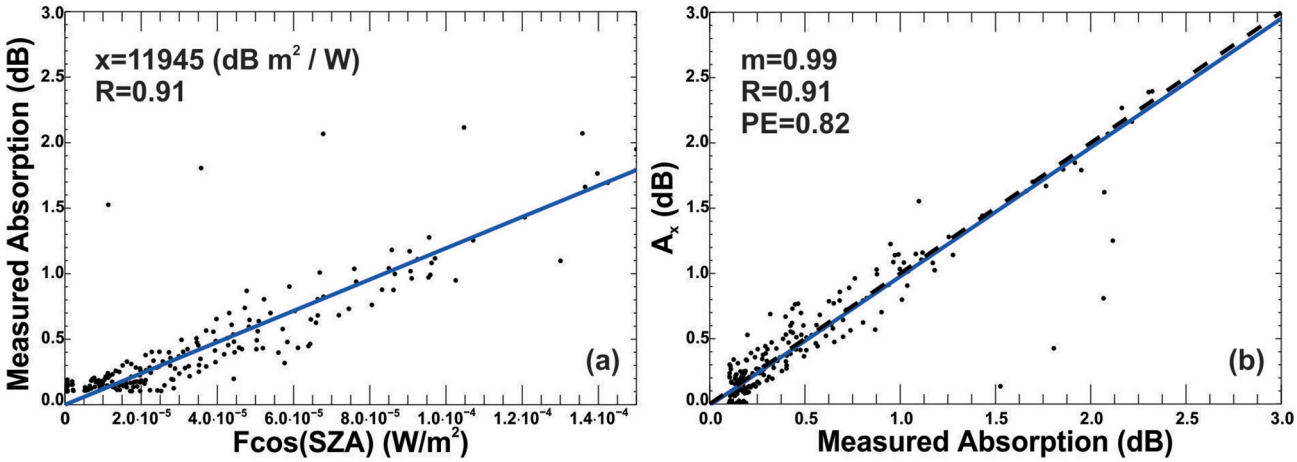

Fig. 3. (a) Scatter plot of absorption measured by the NRCan riometer array versus the product of the solar X-ray flux (F) and the cosine of the solar zenith angle (SZA). The slope of the best-fit line to the data (solid blue line; corresponding to *x* from Eq. (6)) is given by x = 18,676 ± 352 (dB m^2/W). Based on the relationship derived in (a), absorption was modelled from Eq. (6). In (b), the modelled absorption (A_x) is plotted against absorption measured by the NRCan riometer array. The dashed bisector indicates perfect agreement and the solid blue line is the best-fit line to the data set. Data were recorded during an X2.2 solar X-ray flare observed March 11, 2015 for the period bounded in Fig. 2. Slope of the best-fit line to the data (x, m), Pearson correlation coefficient (R), and prediction efficiency (PE) are indicated.

a constant uncertainty of 0.1 dB. Fitting coefficient *x*, the uncertainty in A_x (σ_{Ax}), and the uncertainty in *x* are determined through least-squares fitting as (Taylor, 1997)

$$x = \frac{\sum_i (A_{x_i} F_i cos(SZA_i))}{\sum_i (F_i cos(SZA_i))^2}, \tag{7}$$

$$\sigma_{A_x} = \sqrt{\frac{\sum (A_{x_i} - x\ F_i cos(SZA_i))^2}{N-1}}, \text{ and} \tag{8}$$

$$\sigma_x = \frac{\sigma_{A_x}}{\sum_i (F_i cos(SZA_i))^2}, \tag{9}$$

where N is the number of points to fit.

The cosine term in Eq. (6) causes absorption to be a maximum when the sun is directly overhead (SZA = 0°) and fall off to zero as SZA increases to 90°. As SZA exceeds 90°, the ionosphere shifts from being illuminated from above to being illuminated from below until roughly SZA = 95° (e.g., Turunen et al., 1996). The simplistic model described here is limited to purely dayside absorption from overhead solar illumination and is therefore limited to SZA ≤90°. Evaluation of shortwave fadeout absorption for SZA >90° is recommended for a future study.

Data-based optimization is performed to describe the degradation to a 30 MHz signal for a single representative event on March 11, 2015 and a collection of 87 solar X-ray flare events.

4.1. Event study: March 11, 2015

Solar X-ray flux and riometer data for all available stations for the time period identified in Fig. 2 for the March 11, 2015 were examined using the data-based optimization model described by Eq. (6). Fig. 3a shows a comparison between the measured absorption and *F*cos (*SZA*). In Fig. 3a, measured absorption >0 dB are shown, but only values for measured absorption >0.1 dB are used for calculating statistics to reduce bias in the fit caused by absorption measurements being limited to 0.1 dB. With the exception of 5 outlying points for >1 dB measured absorption, there is excellent agreement between variables, demonstrated by a Pearson correlation coefficient of R = 0.91. The fitting coefficient *x* is 11,945 (m^2 dB/W), shown by the blue line, with a 1-sigma uncertainty (σ_x) estimate of 254 (m^2 dB/W). The least-squared relationship can be used to model absorption through Eq. (6), as shown by the dashed green line (A_x) in Fig. 2b. For data bounded by the red dashed vertical bars in Fig. 2b, the RMSE between A_x and the measured absorption is 0.1 dB for measured absorption >0.1 dB and measured absorption >1.0 dB. This represents a significant improvement over the D-RAP model where RMSE was 1.0 dB for >0.1 dB absorption and 1.5 dB for >1.0 dB absorption.

Fig. 3b shows the resultant comparison between modelled and measured absorption. There is excellent correlation between measured and modelled values; the correlation remains at R = 0.91. The ability of the model to predict measured values is evaluated using the prediction efficiency (PE), which represents the fraction of the variance (Detman and Vassiliadis, 1997; Weimer, 2005). PE is given by

$$PE = 1 - \frac{\sum_{i=1}^{N} (A_{x_i} - A_i)^2}{\sum_{i=1}^{N} (A_i - \overline{A_i})^2} \tag{10}$$

where A_i, A_{x_i}, and $\overline{A_i}$ represent the measured and modelled Eq. (6) absorption for each data point, *i*, and the measured absorption is averaged over the total number of data points (*N*). PE evaluates the ability of a model to represent variation in the data about the mean. A perfect model that demonstrates perfect agreement with measured data will have PE = 1. In this case PE is high at PE = 0.82. The best-fit line to the data has a slope of m = 0.99 indicating the model slightly underestimates the observed absorption, but to a significantly lesser extent than the D-RAP model (m = 0.11; not shown). A scattering of 6 off-center points that forms an arc with measured absorptions of ~1–2 dB for modelled absorptions <2 dB shows a pronounced underestimation by the model. These points are attributed to the SNK riometer, which observed an enhancement onset and peak absorption prior to that observed by all other stations. SNK absorption peaked at 16:19 UT; 3 min prior to the flare peak and ~2 min prior to the peak absorption observed by stations reported in Fiori et al. (2018). The reason for the discrepancy is currently unclear. If the SNK riometer data were removed from the comparison, the statistics improve to *m* = 1.00, R = 0.97, and PE = 0.94.

In the literature (e.g., Table 2), absorption is described as $A \sim cos^y(SZA)$ with *y* varying from 0.2 to 1.29. However, in Eq. (6), *y* has been taken as 1 to simplify the model. The impact of changing the exponent *y* was examined for this event by considering the agreement between measurement and model data values of *y* ranging from 0 to 3 in increments of 0.01. Fig. 4 shows the Pearson correlation coefficient (R) (thin black line) and PE (heavy blue line) determined for a varying exponent. As exponent *y* increases, both R and PE show a pattern of first increasing, plateauing slightly past 1.0 and then decreasing. Plateaus

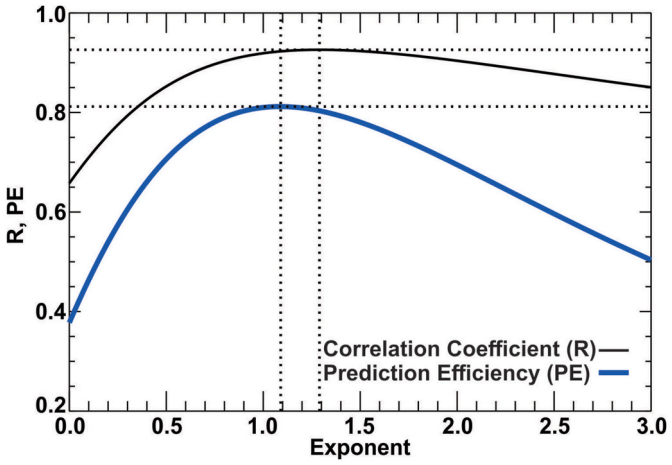

Fig. 4. Agreement between measured absorption and absorption modelled using Eq. (6) where an exponent ranging from 0.0 to 3.0 in increments of 0.01 is applied to the cos (SZA) term. Agreement is characterized by the Pearson correlation coefficient (R) (thin black line) and prediction efficiency (PE) (heavy blue line). Dotted vertical and horizontal lines indicate the x-axis and y-axis values of the peak of the R and PE curves.

peaked at R = 0.93 and PE = 0.81 centered at 1.09 for the PE curve and 1.29 for the R curve. The plateaus in R and PE illustrated in Fig. 4 demonstrate very little change for an exponent near y = 1.00. Therefore, there is very little advantage in selecting, for example, a value of y = 1.00, y = 1.10, or y = 1.20; the R and PE are essentially the same. A subset of 13 events from the multi-event study introduced in the next section (indicated by an asterisk in Table 3) where data are well constrained, such that there are >100 data points, were selected and a similar evaluation performed independently for each event. Maximum correlation was observed to fall between 0.23 and 2.46 (median value of 1.32), and maximum PE was observed to fall between 0.11 and 1.93 (median value of 1.16), in agreement with values reported in Table 2. In each case, plateaus similar to that illustrated for R and PE in Fig. 4 demonstrate very little change in the agreement over a wide range in y. To simplify the model, a value of y = 1.0 was therefore applied. This simplification is in line with Schumer (2009); provided a cosine dependence is applied consistently to the data set, there is no strong advantage to optimizing the cosine dependence as the absorption predictions are determined by first fitting the data to a quiet day curve thus removing the diurnal variation.

4.2. Multi-event study

A multi-event comparison between absorption measured by the NRCan riometer and modelled using both the D-RAP model and the simple data-based optimization model proposed here was performed based on a subset of solar X-ray flares identified from the GOES XRS flare reports between December 2006, when the NRCan riometers came online, and July 2016, when the XRS flare reports end.

The event list was determined by first limiting the GOES XRS reports to events where C, M, or X-class flares were observed while the OTT riometer station was located on the dayside and reported good-quality data not contaminated by radio noise. The OTT station was considered due to the high quality of the data and good continuity of the data set. OTT data for each event were examined by eye to determine whether or not a visible response to the flare was observed following the flare peak. For those events observing a discernible response, data from the 17 riometers illustrated in Fig. 1 were evaluated. An event was included in the study provided the network of NRCan riometers observed at least 10 data points with A>0.1 dB during the solar flare interval. A total of 87 events were included, see Table 3.

Note that in some instances modifications were made to the flare end time. In the GOES XRS files, the end of a flare is defined as the time at which the solar X-ray flux drops half way between the flux at the onset of the flare and the peak flux. Because of the short duration of solar X-ray flare events, this resulted in a small set of data points to constraint the model. Flare end time was defined when at least one of the following conditions were met: a subsequent solar X-ray flare onset was observed, solar X-ray flux dropped below the C1.16 flare level illustrated in the example above, or solar X-ray flux dropped below the level at onset. In some instances the onset of a subsequent solar flux enhancement not identified in the flare catalogue was used to determine end time if the previous conditions were not met. Note that there is no specific

Table 3
Time of peak 0.1–0.8 nm solar X-ray flux and flare class for solar X-ray events considered for constraining the model in the multi-event study. Events marked with an asterisk are referenced in Section 4.1.

Peak	Class	Peak	Class	Peak	Class
2006-12-06 18:47	X6.5	2012-11-21 15:30	M3.5	2014-09-04 16:32	C5.7
2010-01-20 17:55	M3.4	2013-04-05 17:48	M2.2	2014-09-06 17:09	M1.1
2010-02-06 15:39	C3.4	2013-04-12 20:38	M3.3	2014-09-11 15:26	M2.1
2010-10-16 19:12	M2.9	2013-05-12 20:32	M1.9	2014-09-11 21:26	M1.4
2010-11-06 15:36	M5.4	2013-06-07 22:49	M5.9	2014-09-17 19:48	C7.5
2011-02-13 17:30	M6.6	2013-06-23 20:56	M2.9	2014-09-26 16:18	C7.9
2011-02-14 17:26	M2.2	2013-10-25 19:21	M2.3	2014-09-28 18:00	M1.0*
2011-03-08 18:28	M4.4	2013-10-28 14:05	M2.8	2014-10-02 18:15	M1.5*
2011-03-14 19:38	M4.2	2013-10-29 21:54	X2.3	2014-10-02 19:14	M7.3*
2011-09-06 22:20	X2.1	2013-10-31 13:51	M1.9	2014-11-07 17:26	X1.6
2011-09-07 22:38	X1.8	2013-12-22 15:12	M3.3	2014-11-09 15:32	M2.3
2011-09-08 15:46	M6.7	2014-01-30 16:11	M6.6	2014-11-16 17:48	M5.7
2011-09-26 14:46	M2.6*	2014-02-02 18:11	M3.1	2015-03-02 15:28	M3.7
2011-11-03 20:27	X1.9*	2014-04-16 19:59	M1.0	2015-03-02 19:31	M4.1
2012-03-02 17:46	M3.3	2014-06-06 19:31	M1.4	2015-03-09 14:34	M4.5
2012-03-14 15:21	M2.8	2014-06-10 11:42	X2.2	2015-03-11 16:22	X2.1*
2012-04-18 17:06	C5.3	2014-06-10 12:52	X1.5*	2015-03-12 14:04	M4.2
2012-05-07 17:21	C7.4	2014-06-11 21:03	M3.9*	2015-04-21 15:45	M4.0*
2012-05-08 13:08	M1.4	2014-06-12 16:03	C7.8	2015-04-21 17:00	M2.1
2012-05-09 12:32	M4.7	2014-06-12 18:13	M1.3	2015-04-21 21:45	M1.8
2012-05-09 21:05	M4.1	2014-06-12 22:16	M3.1	2015-05-05 17:24	M2.6
2012-07-04 12:24	M2.3	2014-06-14 19:29	M1.4	2015-05-05 22:11	X2.7
2012-07-04 22:09	M4.6	2014-08-01 14:48	M2.0	2015-08-22 21:24	M3.5
2012-07-05 11:44	M6.1	2014-08-21 13:31	M3.4	2015-08-28 13:16	M2.2
2012-07-16 13:10	C2.2	2014-08-21 19:04	C7.3*	2015-08-28 19:04	M2.1
2012-08-17 13:19	M2.4	2014-08-24 12:17	M5.9	2015-09-20 17:57	M2.1
2012-08-18 16:07	M2.0	2014-08-25 15:11	M2.0	2015-10-01 13:10	M4.5
2012-10-20 18:14	M9.0	2014-08-25 20:21	M3.9*	2015-10-02 17:18	M1.0
2012-10-22 18:51	M5.0	2014-09-03 13:54	M2.5*	2016-07-24 17:43	M1.9*

significance to the C1.16 level used; it was selected to allow a long tail such that additional data points could be identified to constrain the model.

To account for minor errors in QDC determination, absorption data were calibrated for each riometer by zeroing the data at the start of the flare interval by removing a constant offset determined as the first 1-min downsampled data point observed within the first 5-min of the event onset.

Solar X-ray flares included in the subset ranged from C2.2 on July 16, 2012 to X6.5 on December 06, 2006; there were 10 C-class events, 68 M-class events, and 9 X-class events. The largest peak absorption (2.4 dB; OTT) was observed for an X2.1 solar X-ray flare when the OTT station was located at 11.5 MLT and SZA = 50.3°. In general, larger peak absorptions were observed for larger events, and a clear response in the riometer observations was not observed for flares < C2.2.

Fig. 5 shows the distribution of the data set in terms of the local time (LT) and SZA location of the NRCan riometer stations for the events considered in the multi-event study. Data spans LTs of 3.7–18.8 and SZAs of 25.2°–104.15° (data are limited to 90° both in the plot, and in the calculations). Data are primarily concentrated on the dayside between 09 LT and 15 LT between 20° and 50°. 'Nightside' LTs were reported only at high SZA by the highest latitude stations where the sun does not set during the summer months. The data set was dominated by the OTT (45.4° geographic latitude) and PEN (49.3° geographic latitude) riometer stations which represent 39% of the overall dataset. This weighting is due to the low-latitude location of these two stations which make them more likely to be impacted by a solar x-ray flare and observe absorption greater than the 0.1 dB threshold. In several instances auroral stations had to be removed from the comparison due to the possibility of contamination of auroral absorption. Auroral absorption was identified as a period of enhanced absorption in conjunction with elevated local magnetic activity (Fiori et al., 2020). The identification of auroral absorption was done on an event-by-event basis by careful examination of the data by eye.

Data for each event at each measurement point was modelled using D-RAP. The D-RAP modelled absorption was shown to severely underestimate the measured absorption. D-RAP modelled absorption values (dB) were, on average, 50% of measured absorption values (dB), consistent with the event demonstrated in Fig. 2. Limiting the data set to measured absorption >0.5 dB and measured absorption >1.0 dB, the D-RAP model absorption values were 24% and 16% of measured absorption values, respectively.

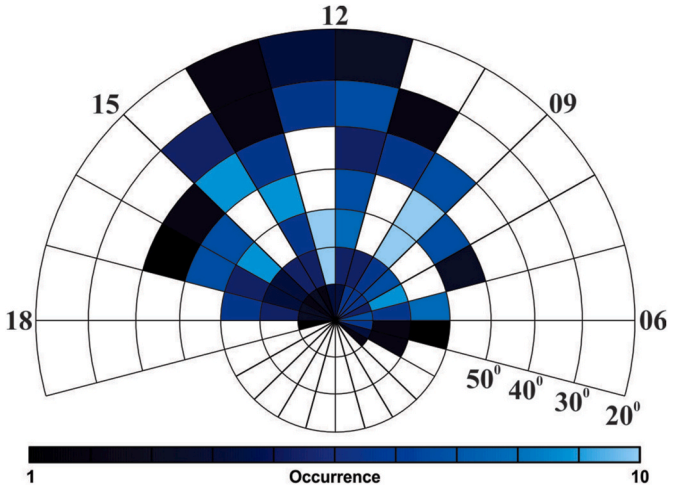

Fig. 5. Local time (LT) and solar zenith angle (SZA) distribution of the location the NRCan riometer stations at the time of the peak solar X-ray flux during the events analyzed in the multi-event study. Data are binned by 1 h of LT and 10° SZA. The number of observations in each bin is indicated by the colour bar. Unshaded LT/SZA bins did not contain stations for any events.

Evaluation of the NRCan model absorption, described by Eq. (6) was expanded by considering data for the 87 events described in the previous section. Parameter x was determined (1) independently for each event (87 separate values of x), and (2) based on the collective data set (one value of x). Statistics, including the Pearson correlation coefficient (R), slope of the line of best fit (x), and prediction efficiency, were evaluated where >0.1 dB absorption was observed.

Fig. 6 shows the distribution of Eq. (6) fitting coefficient (x) and the uncertainty (σ_x; Eq. (9)) when the 87 events were considered independently. Here both x and σ_x are represented using a logarithmic scale due to their range of values. The logarithm of x ranges from 3.70 to 4.86 with a mean value of 4.25, and the σ_x of the logarithm of x ranges from 2.37 to 4.48 with a mean value of 3.01.

Correlation (R) between measured HF absorption and $F\cos(SZA)$ was examined for trends. R varied significantly from −0.70 to 0.98. Of the 87 events examined 58% had R > 0.6. Better correlation tended to be observed for events constrained by > 100 points. Of the 18 events with >100 points, 12 observed R > 0.6. Correlation tended to increase with increasing F; 22% of C-class, 69% of M-class, and 90% of X-class flares observed R > 0.6. In 5 instances R < 0 was observed. For these events data tended to be concentrated near the terminator such that $F\cos(SZA)$ was near zero.

Fig. 7a shows a comparison of absorption independently modelled for each of the 87 events with the corresponding measured absorption. With the exception of the outliers identified for the March 11, 2015 event presented in the previous section, modelled absorption shows excellent agreement with the measured values. The data is closely clustered about the bisecting line and the correlation coefficient is 0.88. A best-fit line to the data has a slope of 0.91 and lies just below the ideal bisector, indicating some underestimation by the model. The prediction efficiency is PE = 0.78 indicating good agreement. There is a small distribution of points where the modelled absorption was <0.1 dB for measured absorption values of up to ~1 dB; these values were not included in calculating the statistics (R and PE). Similar to a χ^2 error statistic, PE is highly sensitive to outliers, explaining why the PE is lower than the correlation and best-fit line suggest. Determination of the best-fit line in this case is done using the method of least absolute deviations (LAD). The LAD approach seeks to minimize the sum of the absolute value of the residuals between measured and modelled data opposed to linear regression which minimize the sum of the squares of the residual. By not squaring the residuals, the LAD approach is less sensitive to outliers than linear regression, explaining the good fit suggested by the slope, despite several outlying points.

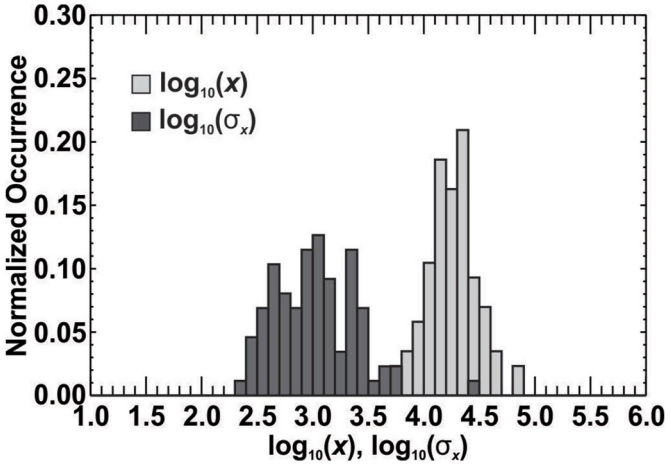

Fig. 6. Distribution of Eq. (6) fitting coefficient (x) (light shading) and uncertainty (σ_x) (dark shading) independently determined using data from the NRCan riometer array and the GOES solar X-ray flux (0.1–0.8 nm) for 87 solar X-ray flare events. Coefficient x has units of (m^2 dB/W).

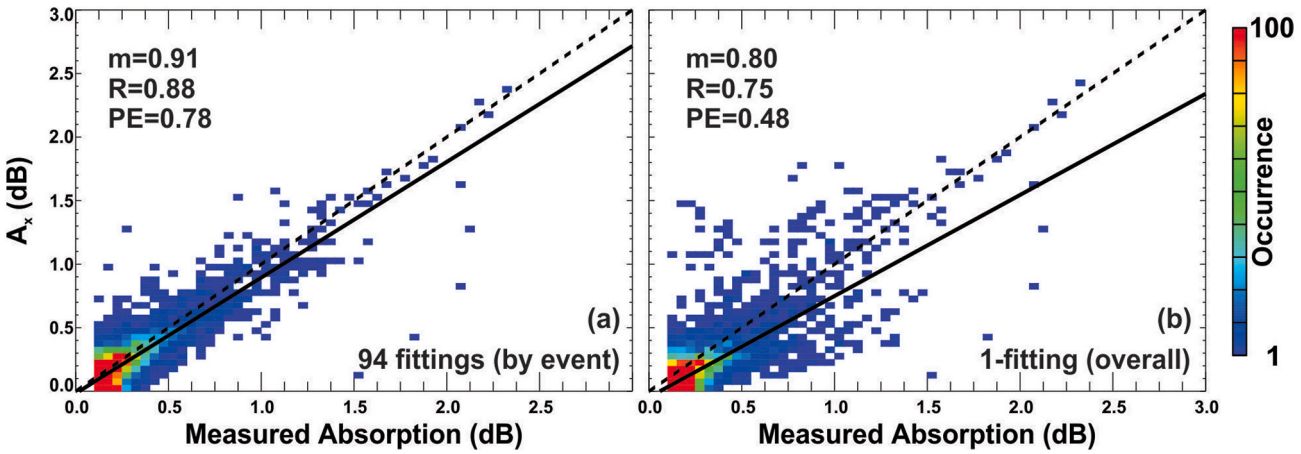

Fig. 7. Scatter plot of model absorption versus measured absorption for 87 solar X-ray flares considered in this study. Data-based optimization of the shortwave fadeout model was performed (a) on an event-by-event basis, and (b) based on the entire data set. Solid black lines represent the best-fit line to the data. Dashed line represents the ideal bisector. The slope of the best-fit line (m), Pearson correlation coefficient (R), and prediction efficiency (PE) are indicated.

Evaluation of the individual models for each event establishes a relationship between absorption and *F*cos (*SZA*) that reliably models measured absorption and by extension, predicts absorption at locations devoid of instrumentation. Data-based optimization of the fitting coefficient (x) relating the two variables (*F*cos (*SZA*) and A_x) is an optimal technique that reflects ionospheric variability not yet being taken into account by the model. Even with physics-based models of the electron density and neutral particle species or the inclusion of radiation transport in the ionosphere (e.g. Zawdie et al., 2017; Levine et al., 2019) it is hard to incorporate the wide array of processes underway in the ionosphere which include the lingering effects of past events which often do not factor into physics-based models. Incorporating data to constrain even a model as simple as that represented by Eq. (6) is a strong approach to modelling the variable state of the ionosphere at the onset of a solar X-ray flare.

However, this data-based optimization approach does require that sufficient data points be available for modelling. For the events presented here, accurate models required >100 dayside observations, preferably for a wide range of *F* and *A*. Such a data set may not be readily available due to the distribution of the riometer stations or the due to the magnitude or duration of the event. Data-based optimization on an event-by-event basis can also fail in the case of real-time modelling until a sufficient number of data points have been collected.

To develop a more general model, data from the entire 87-event data set are considered collectively to develop a single relationship. Absorption and Fcos (SZA) were compared for the overall data set. Correlation was R = 0.77 and the best-fit line to the data had a slope of x = 12,080 (m^2 dB/W) with σ_x = 92 (m^2 dB/W). Fig. 7b shows the relationship between measured and modelled absorption when considering data from all events collectively. Correlation coefficient and slope of the best-fit line to the data have dropped slightly from R = 0.88 and m = 0.91 to R = 0.75 and m = 0.80, but still indicate excellent agreement. There is some underestimation of the model; modelled absorption data are on average 99% of measured values for A > 0.1 dB and 80% of measured values for A > 1 dB. However, this underestimation is considerably reduced compared to the D-RAP model where the modelled absorption data are on average 61% of measured values for A > 0.1 dB and only 16% of measured values for A > 1 dB. Notably though, the prediction efficiency has dropped significantly from PE = 0.78 to PE = 0.48, which is not surprising considering the spread in the data. The generalized absorption model is given by

$$A_x = \left[12080\left(\frac{m^2 dB}{W}\right)\right] F\cos(SZA)\ \ (\mathrm{dB}). \tag{11}$$

Data for an additional 19 events were considered as an independent data set to test the model, see Table 4. The first 18 events for the test data set were selected from periods where the Penticton (PEN) riometer station was located on the dayside and reported good quality data, and the solar X-ray class was ≥M1. For these 18 events the OTT riometer, used to select events for the training data set, either did not observe any observable response to the flare due to a nightside location, or did not collect any high-quality data. The final event is for an X1.3 solar X-ray flare observed September 07, 2017 that occurred during a polar cap absorption event. Only the OTT riometer data was considered for this event as more northern stations were dominated by polar cap absorption. Data for these 19 events were used to model absorption based on solar X-ray flux using the generalized model described by Eq. (11). The results of the comparison between measured and modelled data for the second data set are shown in Fig. 8. The Pearson correlation coefficient is R = 0.83, and the slope of the best-fit line to the data is m = 0.89, and the prediction efficiency is PE = 0.61. There are some points of disagreement where the model overestimates the measured data. However, the overall agreement between measured and modelled data indicates good performance of the model.

5. Discussion

The D-RAP model was originally based on the results of Stonehocker (1970) and using a limited data set confined to summer and noon sector data from one low-latitude station (New Mexico), and describes attenuation of a 5 MHz signal. Setting aside the limitation to the number of events, latitude, and local time, Schumer (2009) points out that scaling

Table 4
Time of peak 0.1–0.8 nm solar X-ray flux and flare class for solar X-ray events considered for testing the model developed in the multi-event study.

Peak	Class	Peak	Class	Peak	Class
2010-02-06 18:59	M2.9	2013-08-17 18:24	M3.3	2014-10-26 18:15	M4.2
2011-11-02 22:01	M4.3	2014-02-25 00:49	X4.9	2015-03-12 21:51	M2.7
2012-03-10 17:44	M8.4	2014-03-13 19:19	M1.2	2015-07-06 20:40	M1.7
2013-05-03 17:32	M5.7	2014-03-28 19:18	M2.0	2015-09-27 21:00	M1.0
2013-05-05 17:56	M1.4	2014-04-25 00:27	X1.3	2015-10-17 20:23	M1.1
2013-05-10 00:57	M3.9	2014-07-10 22:34	M1.5	2017-09-07 16:06	X1.3
2013-05-14 01:11	X3.2				

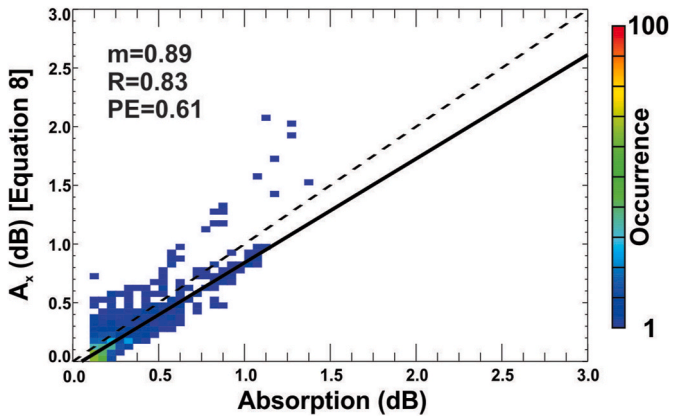

Fig. 8. Scatter plot of absorption modelled from Eq. (11) versus measured absorption for a 21-event test data set described in the text. Solid black line represents the best-fit line to the data. Dashed black line represents the ideal bisector. The slope of the best-fit line (m) and Pearson correlation coefficient (R) are indicated.

absorption by frequency from 5 MHz (Stonehocker study) to 30 MHz (used by D-RAP), see Eq. (4), is largely responsible for the underestimation observed for the D-RAP model. Schumer (2009) showed that the accuracy of the absorption frequency scaling degrades, causing a severe underestimation by the D-RAP SWF model, as frequency increases above the 5 MHz level originally intended. Schumer (2009) showed marked improvement if the frequency scaling were performed using an $z = 1.24$ relationship rather than the $z = 1.5$ relationship imposed by D-RAP, or the $z = 2.0$ value expected for purely non-deviative absorption. Schumer (2009) points out that when the ionospheric electron density is elevated, as it is during a solar flare, ionospheric signals reflect at lower altitudes and there is a greater occurrence of deviative absorption causing a greater discrepancy in the frequency scaling compared to periods of normal electron density.

Recent developments in HF absorption modelling focus on either physics-based or semi-empirical models. While the primary goal of physics-based models is to investigate the dynamics of radiation transport, ionization, ionospheric chemical kinetics, collision frequency, and electron temperature (Levine et al., 2019; Chakraborty et al., 2021), semi-empirical models are used to increase the model forecast skill with the help of physics insight (Eccles et al., 2005). Most of the physics-based models consist of multiple model components including neutral atmosphere, background ionosphere, radiative transport, and wave dispersion relations. The physics-based models estimate enhanced HF absorption by first solving radiative transport equations in the neutral atmosphere to account for enhanced ionization, and then solving wave dispersion equations Eccles et al. (2005); Levine et al., 2019; Chakraborty et al. (2021)]. In comparison, the semi-empirical models estimate enhanced ionization from empirical equations, and then estimate the HF absorption by solving wave dispersion equations (Eccles et al., 2005). Levine et al. (2019) did a comprehensive study on solving the radiative transfer and continuity equations for estimating energy deposition in the upper atmosphere by describing the flare-enhanced solar irradiance as a function of height. Both physics-based and semi-empirical models estimate HF absorption by solving the wave dispersion relation with collision frequency formulations. Chakraborty et al. (2021) investigated which wave dispersion relation and collision frequency formulation most accurately reproduces HF absorption observations. While physics-based models have relatively high accuracy and can provide physical insights, they suffer from low throughput (ratio of model accuracy and runtime). The model described by Chakraborty et al. (2021) takes ~15 min to produce 1-h of riometer observations for one station. This is in contrast with available data-driven HF absorption models. Most data-driven HF absorption models, such as D-RAP, and the data-based optimization method presented here, can be described by simple empirical equations and can produce 2D global HF absorption maps in less than minutes. However, the accuracy of the data-driven models can be lower than physics-based models. Hence, throughput of existing data-driven models can also be low. In this study we describe a new data-driven model with relatively high throughput by increasing accuracy like physics-based models while keeping the runtime of the model comparable to existing data-driven models.

6. Summary and conclusions

This paper presents and evaluates a simplified shortwave fadeout absorption model constrained by 30 MHz riometer data. The model more accurately predicts ionospheric absorption than the D-region absorption prediction (D-RAP) model on which it is based, and is more efficient than physics-based models.

Absorption modelled during a single X2.1 solar X-ray flare on March 11, 2015 was shown to reach only 49%, on average, of the measured values for measured absorption >0.1 dB (RMSE = 0.9 dB), and only 17% of the corresponding measured values for absorption >1 dB (RMSE = 1.4 dB) using the D-RAP model. The data-based optimization model applied here more accurately represents the modelled data causing a 1% overestimation overall for measured absorption >0.1 dB (RMSE = 0.2 dB).

Data for all available riometers in the Canadian NRCan network spanning from 45.4°N to 82.5°N geographic latitude and 225.6°E to 307.3°E geographic longitude were used to constrain a data-based optimized absorption model for 87 events where an absorption response of at least 0.1 dB was observed. Performing the data-based optimization separately for each event, and then comparing measured and modelled absorption showed a good agreement between data sets. The Pearson correlation coefficient and the slope of the best-fit line to the data were R = 0.88 and m = 0.91, respectively. The prediction efficiency was PE = 0.78. Measured and modelled data were considered collectively to create a generalized model. The correlation dropped to R = 0.75 in the generalized model, still indicating good agreement. Slope dropped to m = 0.80 suggesting some underestimation of absorption by the model. The prediction efficiency dropped notably from PE = 0.78 to PE = 0.48. Evaluation of the model using an independent data set showed agreement with the results from the training data set.

This paper demonstrates that the D-RAP model could be significantly improved through the omission of frequency scaling Eq. (4), simplification of the model expression Eq. (11) and the incorporation of riometer data to optimize the model. A data-based optimization approach to modelling is shown to be an effective technique for modelling absorption caused by the variable state of the ionosphere in response to a solar X-ray flare.

Declaration of competing interest

The authors declare that they have no known competing financial interests or personal relationships that could have appeared to influence the work reported in this paper.

Acknowledgements

This work was supported by the Natural Resources Canada (NRCan) (1) Lands and Minerals Sector, Canadian Hazards Information Service, and (2) Earth Sciences Sector, Public Safety Geosciences program. SC thanks the National Science Foundation and NASA for support under grant AGS-1935110 and 80 NSSC20K1380, respectively. GOES solar X-ray flux data are available from the National Geophysical Data Center (NGDC) (http://www.ngdc.noaa.gov/stp/satellite/goes/dataaccess.html). NRCan riometer data are available from Fiori (2021). This is NRCan publication 20210218.

References

Agy, V., 1970. HF radar and auroral absorption. Radio Sci. 5 (11), 1317–1324. https://doi.org/10.1029/RS005i011p01317.

Bajcetic, J., Nina, A., Cadez, V., Todorovic, B., 2015. Ionospheric D-region temperature relaxation and its influences on radio signal propagation after solar X-flares occurrence. Therm. Sci. 19 https://doi.org/10.2298/TSCI141223084B.

Barnes, et al., 2016. A comparison of flare forecasting methods. I. Results from the "all-clear" workshop. Astrophys. J. 829 (2) https://doi.org/10.3847/0004-637X/829/2/89.

Belrose, J.S., Cetiner, E., 1962. Measurement of electron densities in the ionospheric D-region at the time of a 2+ solar flare. Nature 196, 688–690.

Berngardt, O.I., Ruohoniemi, J.M., Nishitani, N., Shepherd, S.G., Bristow, W.A., Miller, E. S., 2018. Attenuation of decameter wavelength sky noise during x-ray solar flares in 2013-2017 based on the observations of midlatitude radars. J. Atmos. Sol. Terr. Phys. 173, 1–13. https://doi.org/10.1016/j.jastp.2018.03.022.

Bibl, K., Paul, A., Rawer, K., 1961. Absorption in the D and E regions and its time variation. J. Atmos. Sol. Terr. Phys. 23 https://doi.org/10.1016/0021-9169(61)90049-6.

Bland, E.C., Heino, E., Kosch, M.J., Partamies, N., 2018. SuperDARN radar-derived HF radio attenuation during the September 2017 solar proton events. Space Weather 16, 1455–1469. https://doi.org/10.1029/2018SW001916, 2018.

Brodrick, D., Tingay, S., Wieringa, M., 2005. X-ray magnitude of the 4 November 2003 solar flare inferred from the ionospheric attenuation of the galactic radio background. J. Geophys. Res. 110 (A09S36) https://doi.org/1029/2004JA010960.

Browne, S., Hargreaves, J.K., Honary, B., 1995. An imaging riometer for ionospheric studies. Electron. Commun. Eng. J. 7 (5), 209–217. https://doi.org/10.1049/ecej:19950505.

Cannon, P., Angling, M., Barclay, L., Curry, C., Dyer, C., Edwards, R., Greene, G., Hapgood, M., Horne, R., Jackson, D., Mitchell, C., Owen, J., Richards, A., Rogers, C., Ryden, K., Saunders, S., Sweeting, M., Tanner, R., Thomson, A., Underwood, C., 2013. Extreme Space Weather: Impacts on Engineered Systems and Infrastructure. Royal Academy of Engineering, London.

Chakraborty, S., Ruohoniemi, J.M., Baker, J.B.H., Nishitani, N., 2018. Characterization of short-wave fadeout seen in daytime SuperDARN ground scatter observations. Radio Sci. 53 (4), 472–484. https://doi.org/10.1002/2017RS006488.

Chakraborty, S., Baker, J.B.H., Ruohoniemi, J.M., Kunduri, B.S.R., Nishitani, N., Shepherd, S.G., 2019. A study of SuperDARN response to co-occurring space weather phenomena. Space Weather 17, 1351–1363. https://doi.org/10.1029/2019SW002179.

Chakraborty, S., Baker, J.B.H., Fiori, R.A.D., Ruohoniemi, J.M., Zawdie, K.A., 2021. A model framework to estimate ionospheric HF absorption produced by solar flares. Radio Sci. 56 (10) https://doi.org/10.1029/2021RS007285.

Chisham, G., et al., 2007. A decade of the Super Dual Auroral Radar Network (SuperDARN): scientific achievements, new techniques and future directions. Surv. Geophys. 28 (1), 33–109. https://doi.org/10.1007/s10712-007-9017-8.

Contreira, D.B., Rodrigues, F.S., Makita, K., Brum, C.G.M., Gonzalez, W., Trivedi, N.B., da Silva, M.R., Schuch, N.J., 2005. An experiment to study solar flare effects on radio-communication signals. Adv. Space Res. 36, 2455–2459. https://doi.org/10.1016/j.asr.2004.03.019.

Special topics in HF propagation. In: Coyne, V.J. (Ed.), 1979. AGARD Conf. Proc. No. 263. Advisory Group for Aerospace Research and Development, North Atlantic Treaty Organization.

Danskin, D.W., Koustov, A.V., Ogawa, T., Nishitani, N., Nozawa, S., Milan, S.E., Lester, M., Andre, D., 2002. On the factors controlling occurrence of F-region coherent echoes. Ann. Geophys. 20, 1385–1397. https://doi.org/10.5194/angeo-20-1385-2002.

Danskin, D.W., Boteler, D., Donovan, E., Spanswick, E., 2008. The Canadian riometer array. In: Proc. Of the 12th International Ionospheric Effects Symposium, IES 2008.

Davies, K., 1990. Ionospheric Radio, IEE Electromagn, vol. 31. Ser. Peter Peregrinus, London.

Detman, T.R., Vassiliadis, D., 1997. Review of techniques for magnetic storm forecasting. In: Tsurutani, B.T., et al. (Eds.), Magnetic Storms, Geophys. Monogr. Ser., vol. 98. AGU, Washington, D. C., pp. 253–266

Eccles, J.V., Hunsucker, R.D., Rice, D., Sojka, J.J., 2005. Space weather effects on mid-latitude HF propagation paths: observations and a data-driven D-region model. Space Weather 3 (1). https://doi.org/10.1029/2004SW000094.

Fiori, R.A.D., 2021. Riometer Data for: Data-Based Optimization of a Simple Shortwave Fadeout Absorption Model. Harvard Dataverse. https://doi.org/10.7910/DVN/8QPL75 vol. 1.

Fiori, R.A.D., Danskin, D.W., 2016. Examination of the relationship between riometer-derived absorption and the integral proton flux in the context of modeling polar cap absorption. Space Weather 14, 1032–1052. https://doi.org/10.1002/2016SW001461.

Fiori, R.A.D., Koustov, A.V., Chakraborty, S., Ruohoniemi, J.M., Danskin, D.W., Boteler, D.H., Shepherd, S.G., 2018. Examining the potential of the super dual auroral radar network for monitoring the space weather impact of solar X-ray flares. Space Weather 16, 1348–1362. https://doi.org/10.1029/2018SW001905.

Fiori, R.A.D., Trichtchenko, L., Balch, C., Spanswick, E., Groleau, S., 2020. Characterizing auroral-zone absorption based on global Kp and regional geomagnetic hourly range indices. Space Weather 18 (12). https://doi.org/10.1029/2020SW002572.

Frissell, N.A., Miller, E.S., Kaeppler, S.R., Ceglia, F., Pascoe, D., Sinanis, N., Smith, P., Williams, R., Shovkoplyas, A., 2014. Ionospheric sounding using real-time amateur radio reporting networks. Space Weather 12, 651–656. https://doi.org/10.1002/2014SW001132.

Frissell, N.A., Vega, J.S., Markowitz, E., Gerrard, A.J., Engelke, W.D., Erickson, P.J., Miller, E.S., Luetzelschwab, R.C., Bortnik, J., 2019. High-frequency communications response to solar activity in September 2017 as observed by amateur radio networks. Space Weather 17 (1), 118–132. https://doi.org/10.1029/2018SW002008.

Hosokawa, K., Iyemori, T., Yukimatu, A.S., Sato, N., 2000. Characteristics of solar flare effect in the high-latitude ionosphere as observed by the SuperDARN radars. Adv. Polar Up. Atmos. Res. 14, 66–75.

Hunsucker, R.D., Hargreaves, J.K., 2003. The High-Latitude Ionosphere and its Effects on Radio Propagation, Cambridge Atmospheric and Space Science Series. Cambridge University Press, Cambridge.

Kikuchi, T., Sugiuchi, H., Ishimine, T., Maeno, H., Honma, S., 1986. Solar-terrestrial disturbances of June-September 1982. IV. Ionospheric disturbances. 1. HF Doppler observations. J. Radio Res. Lab. 33 (1), 239–255.

Knipp, D.J., Bernstein, V., Wahl, K., Hayakawa, H., 2021. Timelines as a tool for learning about space weather storms. J. Space Weather Space Clim. 11 (29) https://doi.org/10.1051/swsc/2021011.

Lam, H.-L., 2011. From early exploration to space weather forecasts: Canada's geomagnetic odyssey. Space Weather 9. https://doi.org/10.1029/2011SW000664.

Levine, E.V., Sultan, P.J., Teig, L.J., 2019. A parameterized model of X-ray solar flare effects on the lower ionosphere and HF propagation. Radio Sci. 54, 168–180. https://doi.org/10.1029/2018RS006666.

Machol, J., Viereck, R., 2016. GOES X-Ray Sensor (XRS) Measurements. https://ngdc.noaa.gov/stp/satellite/goes/doc/GOES_XRS_readme.pdf. (Accessed 15 October 2021).

Mitra, A., 1974. Ionospheric Effects of Solar Flare, vol. 46. Astrophysics and space science library, Massachusetts: Reading. https://doi.org/10.1007/978-94-010-2231-6.

NASA, 2006. GOES N Data Book, CDRL PM-1-1-03, Revision B. February 2005. https://www.nasa.gov/pdf/148080main_GOES-N%20Databook%20with%20Copyright.pdf. (Accessed 15 October 2021).

National Research Council, 2008. Severe Space Weather Events – Understanding Societal and Economic Impacts: a Workshop Report. Natl. Acad. Press, Washington, D.C., p. 144

Neal, J.J., Rodger, C.J., Green, J.C., 2013. Empirical determination of solar proton access to the atmosphere: impact on polar flight paths. Space Weather 11, 420–4333. https://doi.org/10.1002/swe.20066.

NORSTAR, 2014. CANOPUS quiet day curve generation. Available online: http://aurora.phys.ucalgary.ca/norstar/rio/doc/CANOPUS_Riometer_Baselining.pdf. (Accessed 29 March 2020).

Oyinloye, J.O., 1978. On the seasonal variation of absorption of radio waves in the equatorial ionosphere. J. Atmos. Terr. Phys. 40, 793–798. https://doi.org/10.1016/0021-9169(78)90030-2.

Pirjola, R., Kauristie, K., Lappalainen, H., Viljanen, A., Pulkkinen, A., 2005. Space weather risk. Space Weather 3 (S02A02). https://doi.org/10.1029/2004SW000112.

Redmon, R.J., Seaton, D.B., Steenburgh, R., He, J., Rodriguez, J.V., 2018. September 2017's geoeffective space weather and impacts to Caribbean radio communications during hurricane response. Space Weather 16, 1190–1201. https://doi.org/10.1029/2018SW001897.

Rodger, C.J., Molchanov, O.A., Thomson, N.R., 1998. Relaxation of transient ionization in the lower ionosphere. J. Geophys. Res. 103 (A4) https://doi.org/10.1029/98JA00016.

Rogers, N.C., Honary, F., 2015. Assimilation of real-time riometer measurements into models of 30 MHz polar cap absorption. J. Space Weather Space Clim. 5, 1–18. https://doi.org/10.1051/swsc/2015009.

Sauer, H., Wilkinson, D.C., 2008. Global mapping of ionospheric HF/VHF radio wave absorption due to solar energetic protons. Space Weather 6, S12002. https://doi.org/10.1029/2008SW000399.

Schumer, E.A., 2009. Improved Modeling of Midlatitude D-Region Ionospheric Absorption of High Frequency Radio Signals during Solar X-Ray Flares, PhD Dissertation, AFIT/DS/ENP/09-J01, U.S. Air Force. Wright-Patterson Air Force Base, Ohio.

Schwentek, H., 1961. Short wave fadeouts, their modes and complete characterization. J. Atmos. Terr. Phys. 23, 68–84. https://doi.org/10.1016/0021-9169(61)90033-2.

Sigernes, F., Dyrland, M., Brekke, P., Chernouss, S., Lorentzen, D.A., Oksavik, K., Ceehr, C.S., 2011. Two methods to forecast auroral displays. J. Space Weather Space Clim. 1 (A03) https://doi.org/10.1051/swsc/2011003.

Stonehocker, G.H., 1970. Advanced telecommunication forecasting technique in AGY, 5th., Ionospheric forecasting. AGARD (Advis. Group Aerosp. Res. Dev) Conf. Proc. 29, 27–31.

Swalwell, B., Dalla, S., Kahler, S., White, S.M., Ling, A., Viereck, R., Veronig, A., 2018. The reported durations of GOES soft X-ray flares in different solar cycles. Space Weather 16 (6), 660–666. https://doi.org/10.1029/2018SW001886.

Taylor, J.R., 1997. An Introduction to Error Analysis: the Study of Uncertainties in Physical Measurements, second ed. University Science Books, Sausalito, California.

Thayaparan, T., Ibrahim, Y., Polak, J., Riddolls, R., 2018. High-frequency over-the-horizon-radar in Canada. IEEE Trans. Geosci. Rem. Sens. 15 (11), 1700–1704. https://doi.org/10.1109/LGRS.2018.2856185.

Turunen, E., Matveinen, H., Tolvanen, J., Ranta, H., 1996. D-region ion chemistry model. In: Schunk, R.W. (Ed.), Solar-Terrestrial Energy Program: Handbook of Ionospheric Models. SCOSTEP Secretariat, Boulder, Colorado, pp. 1–26.

Watanabe, K., Nishitani, N., 2013. Study of ionospheric disturbances during solar flare events using the SuperDARN Hokkaido radar. Adv. Polar Sci. 24 (1), 12–18. https://doi.org/10.3724/SP.J.1085.2013.00012.

Weimer, D., 2005. Predicting surface geomagnetic variations using ionospheric electrodynamic models. J. Geophys. Res. 110 (A12307) https://doi.org/10.1029/2005JA011270.

Zawdie, K.A., Drob, D.P., Siskind, D.E., Coker, C., 2017. Calculating the absorption of HF radio waves in the ionosphere. Radio Sci. 52, 767–783. https://doi.org/10.1002/2017RS006256.

Preflight Results

Document Information

Title: Data-based optimization of a simple shortwave fade...
Author: R.A.D. Fiori
Creator: Elsevier
Producer: Acrobat Distiller 8.1.0 (Windows)

Preflight Information

Profile: Convert to PDF/A-1b
Version: Qoppa jPDFPreflight v2021R1.00
Date: May 20, 2022 10:52:39 AM

Legend: (X) - Can NOT be fixed by PDF/A-1b conversion.
(!X) - Could be fixed by PDF/A-1b conversion. User chose to be warned in PDF/A settings.

Page 3 Results

(X) Font widths must be the same in both the font dictionary and the embedded font file.
(X) Font widths must be the same in both the font dictionary and the embedded font file.
(X) Font widths must be the same in both the font dictionary and the embedded font file.
(X) Font widths must be the same in both the font dictionary and the embedded font file.
(X) Font widths must be the same in both the font dictionary and the embedded font file.
(X) Font widths must be the same in both the font dictionary and the embedded font file.
(X) Font widths must be the same in both the font dictionary and the embedded font file.
(X) Font widths must be the same in both the font dictionary and the embedded font file.
(X) Font widths must be the same in both the font dictionary and the embedded font file.
(X) Font widths must be the same in both the font dictionary and the embedded font file.
(X) Font widths must be the same in both the font dictionary and the embedded font file.

Page 4 Results

(X) Font widths must be the same in both the font dictionary and the embedded font file.
(X) Font widths must be the same in both the font dictionary and the embedded font file.
(X) Font widths must be the same in both the font dictionary and the embedded font file.
(X) Font widths must be the same in both the font dictionary and the embedded font file.
(X) Font widths must be the same in both the font dictionary and the embedded font file.
(X) Font widths must be the same in both the font dictionary and the embedded font file.
(X) Font widths must be the same in both the font dictionary and the embedded font file.

Page 5 Results

(X) Font widths must be the same in both the font dictionary and the embedded font file.
(X) Font widths must be the same in both the font dictionary and the embedded font file.
(X) Font widths must be the same in both the font dictionary and the embedded font file.
(X) Font widths must be the same in both the font dictionary and the embedded font file.
(X) Font widths must be the same in both the font dictionary and the embedded font file.

Page 7 Results

(X) Font widths must be the same in both the font dictionary and the embedded font file.